Particle Size Matters – Impact of Particle Size and Crucible Geometry on Sublimation Behavior of Formamidinium Iodide

Alexander Diercks[a+*], *Julian Petry*[b+*], *Thomas Feeney*[a], *Richard Thelen*[b], *Paul Fassl*[a,b*] *and Ulrich W. Paetzold*[a,b*]

a *Light Technology Institute, Karlsruhe Institute of Technology, Engesserstrasse 13, 76131 Karlsruhe, Germany*
b *Institute of Microstructure Technology, Karlsruhe Institute of Technology, Hermann-von-Helmholtz-Platz 1, 76344 Eggenstein-Leopoldshafen, Germany*

E-mail: alexander.diercks@kit.edu; julian.petry@kit.edu; paul.fassl@kit.edu; ulrich.paetzold@kit.edu

Funding: ((Please include all funding sources including grant numbers))

Keywords: thermal evaporation, vapor phase deposition, formamidinium iodide, sublimation behavior, perovskite solar cells, thermal sublimation, vacuum process

(Alexander Diercks and Julian Petry contributed equally to this work.)

Abstract

Vapor phase deposition processes for the fabrication of perovskite solar cells show great potential for transferring from laboratory-scale to continuous industrial-scale production. Precise process control and high process reproducibility are of utmost importance to unlock their full potential. In this regard, the sublimation behavior and rate control of organic precursor materials in thermal evaporation processes are particularly challenging. Here, we investigate in detail how the particle size of formamidinium iodide (FAI) and the crucible geometry influence the directionality of the emitted vapor flux. We show that conical crucibles lead to beam focusing of the vapor flux, while cylindrical crucibles show a broader, less directional emission profile. This leads to differences in the homogeneity of material deposition depending on the lateral source-to-substrate distance. Furthermore, there is a substantial impact of FAI particle size on the directionality of the vapor flux for conical crucibles, affecting the deposited material thickness gradient over the substrate. Analyzing commonly employed inorganic materials reveals the strong material dependence of effusion characteristics, leading to additional complexity for multi-material deposition processes. Our findings emphasize that both homogenization of organic precursor materials and optimization of source geometry and arrangement are critical for achieving uniform deposition and, consequently, improved process reproducibility.

1. Introduction

Metal halide perovskite solar cells (PSCs) have emerged as one of the most promising candidates for next-generation photovoltaic technologies due to their exceptional optoelectronic properties and steep increase in reported power conversion efficiencies (PCEs).[1–4] Over the past 15 years, the PCE of PSCs has steadily increased to certified PCEs of up to 26.95%, drawing significant attention from both academic and industrial communities.[5] Most research on PSCs focuses on solution-based deposition techniques, with less than 2% of all publications reporting on vapor-based deposition methods.[6] However, vapor phase deposition offers several advantages regarding the fabrication of high-quality perovskite thin films.[6–8] Conformal coverage and film growth over non-planar substrates is crucial for tandem photovoltaics on textured silicon wafers and sets it apart from solution-based fabrication processes.[9–11] In addition, the ability to produce uniform films over large areas makes vapor phase deposition a promising candidate for high-throughput and continuous in-line processing, critical for cost-effective upscaling and commercialization.[8,12]

Despite their advantages, key challenges remain for further advancing vapor phase deposition processes for PSCs. It is commonly known that the two most employed vapor-based methods, co-deposition and sequential deposition in high vacuum, suffer from reproducibility and repeatability problems, including difficulties in transferring processes from one system to another. This is because the properties of thermally sublimed perovskite films and the resulting device performance are highly sensitive to factors such as the underlying substrate,[13–17] deposition conditions (e.g., chamber pressure, substrate temperature, deposition rate),[15,18–22] film stoichiometry[14,16,20,23,24] and precursor impurities.[21,25,26] One reason leading to such variations is the sublimation behavior and resulting difficult process control of the commonly employed organic precursor materials methylammonium iodide (MAI) and formamidinium iodide (FAI).[21,26,27] In recent years, FA-based PSCs have demonstrated higher PCEs and superior stability compared to their MA-based counterparts,[28] resulting in a trend within the research community towards focusing on pure FA-based compositions.[6,29] While the non-directional sublimation behavior of MAI and its effect on device performance has been studied in much detail,[14,15,18,20,23–26,30,31] fundamental studies for the case of FAI are scarce.[16,19,21] A more profound understanding for reproducibility problems in thermally sublimed FA-based PSCs is therefore essential for the further advancement of highly efficient and stable vapor-phase-deposited PSCs.[21] In this regard, there are currently no studies on the effects of different precursor particle sizes and sublimation crucible geometries, both of which could impact the

sublimation behavior and effusion characteristics, and thus device performance and reproducibility.

In response, this work focuses on a detailed analysis of FAI sublimation behavior in terms of precursor particle size and sublimation crucible geometries to improve and understand process control for vapor-phase-deposited PSCs. We find that both the particle size of commercially available FAI precursor material and the sublimation crucible geometry have a significant effect on the directionality of the emitted vapor flux and, consequently, the effective deposition rate on the substrate. Substantial inconsistencies in the particle size distribution of commercial FAI precursor material are observed between different synthesis batches as well as amongst different bottles from the same synthesis batch. Using three defined particle size fractions for sublimation of FAI, we analyze the deviation of deposited material thickness with respect to the lateral distance of the substrate to the source. We observe a pronounced effect of the particle size fraction on the directionality of the emitted vapor flux when using conical crucibles for the deposition process, which is significantly reduced in the case of cylindrical crucibles. Furthermore, we experimentally compare the vapor flux directionality for commonly employed inorganic materials (lead iodide (PbI_2) and cesium iodide (CsI)), revealing that effusion characteristics are highly material dependent. Our results underscore the importance of precursor material preconditioning, crucible geometry and chamber design for laboratory-scale vapor phase deposition processes, all of which may be a contributing factor to the previously reported inconsistent process reproducibility. Finally, we propose an optimized source arrangement in the vacuum chamber to improve material composition homogeneity for a simulated co-deposition process.

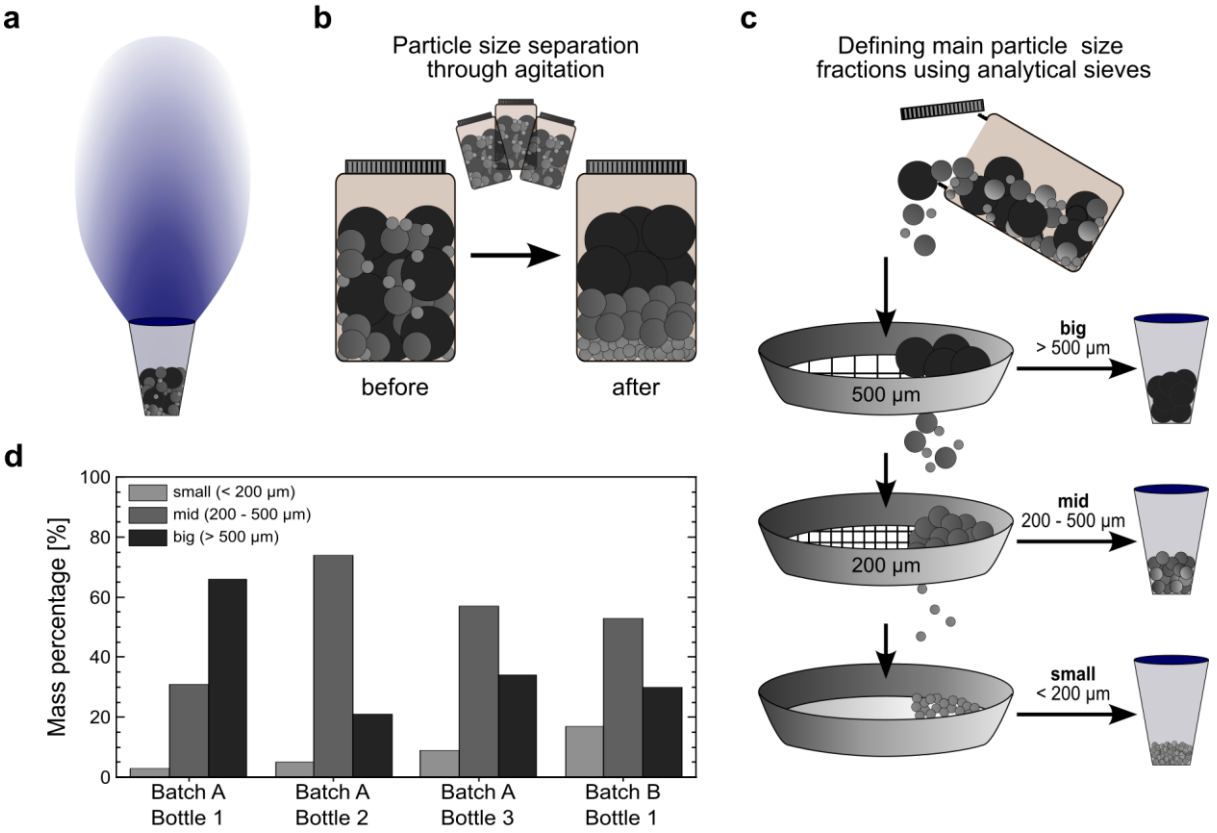


Figure 1: a Illustration of the FAI vapor flux emitted from a conical sublimation crucible. **b** Schematic illustration of granular convection process ("Brazil-nut effect") showing de-mixing effects of different particle sizes in dry powders from material agitation inside a precursor bottle. **c** Illustration of the process to define main particle size fractions (small: x < 200 µm, mid: 200-500 µm and big: x < 500 µm) using analytical sieves of different mesh-sizes**. d** Particle size distribution of FAI from Greatcell Solar Materials in different bottles and fabrication batches (A/B).

2. Results and Discussion

Most reports in literature on FA-based thermal sublimation processes (co-deposition and sequential deposition) use commercially available FAI from Greatcell Solar Materials as the organic cation source (see **Table S1**), which was selected for this study.[16,17,21,32–53] **Figure 1a** exemplary illustrates the vapor flux of FAI emitted from a conical crucible. We analyzed the particle size distribution of FAI powder and found a broad particle size distribution in a single precursor bottle (see **Figure S1**). The control of particle size distribution used in the sublimation processes is inherently challenging, since typically the precursor material is transferred manually from the precursor bottle (usually with a spatula) into the sublimation crucible. Therefore, the particle size distribution inside the sublimation crucible is expected to vary between experiments due to granular convection of the material inside the precursor bottle as an effect of agitation. **Figure 1b** displays a schematic of the granular convection process, commonly referred to as "Brazil-nut effect", to visualize the de-mixing effect from material agitation inside the precursor material bottle. Changes in particle size distribution lead to

inconsistent experimental conditions, potentially affecting reproducibility of the sublimation process. Using analytical sieves of different mesh sizes, three main particle size fractions are defined in this work: small (x < 200 µm), mid (200 - 500 µm) and big (x > 500 µm) (see **Figure 1c**). In fact, we not only found that the FAI particle size distribution changes significantly between different synthesis batches, but even between different bottles of the same synthesis batch (see **Figure 1d**). In addition to the above-discussed various factors that affect perovskite film formation, these inconsistencies in the properties of commercial precursor material add complexity to reproducible processing in laboratory-scale setups.

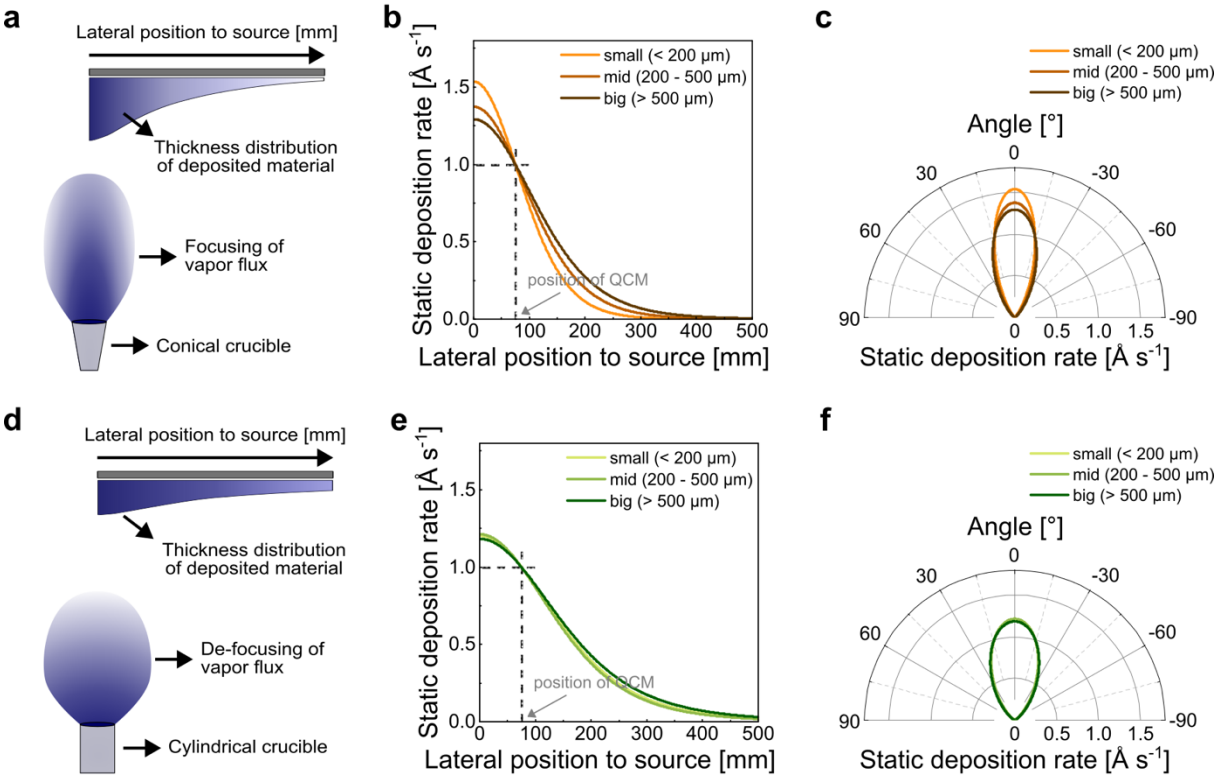


Figure 2: a/d Schematic of the FAI vapor flux and deposition on the substrate from a conical and cylindrical crucible, respectively. **b/e** Comparison of fitted static deposition rate profiles as a function of lateral position to the source for conical and cylindrical crucibles, respectively. **c/f** Angular emission dependence on particle size for conical and cylindrical crucibles, respectively.

To investigate how different particle size fractions and crucible geometries affect the sublimation behavior of FAI, we examine the effusion characteristics of the three defined particle size fractions for two commonly employed types of crucibles (conical vs. cylindrical). **Figure 2a/d** illustrates the vapor flux from a conical and cylindrical crucible, respectively. Static deposition on a non-rotating substrate holder with a quartz-crystal microbalance (QCM)-measured deposition rate of 1 Å s^{-1} leads to a material thickness gradient as shown in **Figure S2 and Figure S3**. The static deposition rate profile is fitted from the experimentally

measured FAI thicknesses across the substrate, as described in our previous work (see **Table S2, Figure S2 and Figure S3**).[54] For a conical crucible, the static deposition rate profile is strongly affected by the particle size fraction (**Figure 2b**). Considering that the particle size distribution in commercial FAI powder varies strongly as discussed above, significant deviations in the effective deposition rate on the substrate holder between experiments are expected, which negatively impacts process repeatability and reproducibility. In comparison, the static deposition rate profiles for a cylindrical crucible are almost identical, making its vapor flux directionality largely independent of the particle size fraction (**Figure 2e**). To summarize, conical crucible geometries lead to beam focusing of the emitted vapor flux that is dependent on the particle size of the precursor material, while cylindrical crucible geometries exhibit a less directional vapor flux that is independent of particle size (see **Figure 2c/f**). These findings highlight the importance of controlling the particle size distribution of the precursor material to achieve reproducible sublimation in vacuum, especially when using conical crucibles. Furthermore, our results show that the crucible geometry in vapor phase deposition processes plays a crucial role on process repeatability, as it can result in variations of the effective deposition rate on the substrate holder for a constant measured deposition rate.

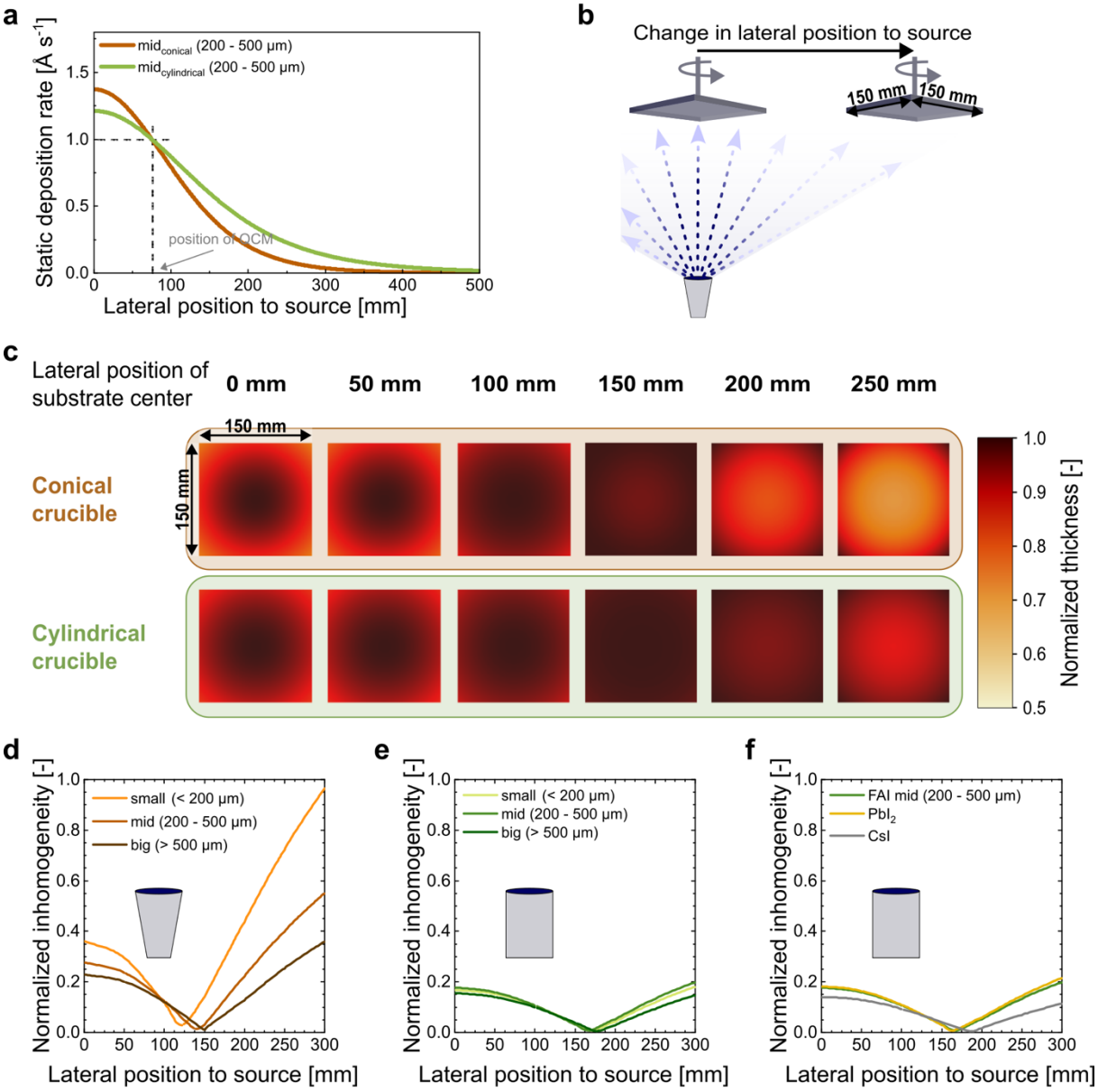


Figure 3: a Comparison of static deposition rates of mid particle size fraction from conical and cylindrical crucible, taken from **Figure 2b/e**. **b** Schematic display to demonstrate the simulated lateral movement of the substrate holder with respect to the emitting source (exemplary displayed as a conical crucible). **c** Heatmaps of calculated thickness distribution (normalized) over a rotating substrate holder at different lateral positions to source (0 mm, 50 mm, 100 mm, 150 mm, 200 mm, 250 mm). **d/e/f** Normalized thickness inhomogeneity as a function of lateral position to source (see Equation (1)) over a rotating substrate holder for different FAI particle size fractions for conical (**d**) and cylindrical (**e**) crucibles, as well as comparison for CsI, PbI_2 and FAI from cylindrical crucibles (**f**).

To understand the effect of crucible geometry and source arrangement, the homogeneity of FAI material deposition from conical and cylindrical crucibles is analyzed concerning the lateral distance from the source to the substrate holder (see **Figure 3a**). We extract the material thickness gradient from the static deposition rate profiles at different lateral positions, maintaining the vertical distance to simulate deposition on a substrate with dimensions of 150 mm x 150 mm. Here, the lateral position refers to the lateral distance between the center of

the emitting source and the center of the substrate (see **Figure 3b;** conical crucible shown for illustrative purposes). The extracted material thickness gradient is rotated 360° over the center of the substrate to simulate a full rotation during deposition and to derive the spatial distribution of material thickness over the whole substrate. **Figure 3c** shows the normalized heatmap profiles for each chosen position and crucible geometry. The resulting heatmaps from deposition from a conical crucible show significant thickness variations from center to edge of the substrate for every substrate position, as well as differences when comparing the individual substrate positions from 0 mm to 250 mm. Meanwhile, heatmaps derived from depositions from a cylindrical crucible appear to be more homogeneous at all substrate positions. The magnitude of these variations is visualized by plotting the diagonal profiles over the substrate for each heatmap as shown in **Figure S5**. Similar results are obtained for the other particle size fractions (see **Figure S4**, **S6** and **S7**). Using the diagonal profile, the magnitude of variation can be quantified for each source position by calculating the normalized thickness inhomogeneity:

$$Normalized\ inhomogeneity\ [-] = \frac{(thickness_{max} - thickness_{min})}{thickness_{mean}} \quad (1)$$

By calculating this variable with respect to substrate holder position, the point of most homogeneous deposition over the entire substrate as a function of the lateral distance between the substrate holder and the emitting source can be derived. In case of deposition from a conical crucible, large shifts in the point of most homogeneous deposition can be seen depending on the used particle size fraction, ranging from 122 mm for small, 137 mm for mid and 149 mm for big particle sizes (see **Figure 3d**). Conversely, deposition from a cylindrical crucible only shows a slight difference in the point of most homogeneous deposition depending on the utilized particle size fraction (small = 171 mm, mid = 168 mm, and big = 177 mm) as shown in **Figure 3e**. We further compared the effusion characteristics of the inorganic materials CsI and PbI_2 from cylindrical crucibles, taken from our previous work,[12] to FAI and extended the analysis and calculations based on the here developed procedure. The corresponding normalized diagonal profiles of the material thickness over the substrate at different lateral positions of the substrate holder to the source are plotted in **Figure S8**. The normalized thickness inhomogeneity is plotted in **Figure 3f** and shows that the point of most homogeneous deposition is at lateral distances of 185 mm and 165 mm for CsI and PbI_2, respectively. These results clearly demonstrate that effusion characteristics are not only dependent on the precursor particle size and the employed crucible geometry but also exhibit a strong dependence on the sublimed material. Changes in the point of most homogeneous deposition can lead to inhomogeneous precursor thickness ratios over the whole substrate when working with multi-material compositions, even when the substrate undergoes rotation.

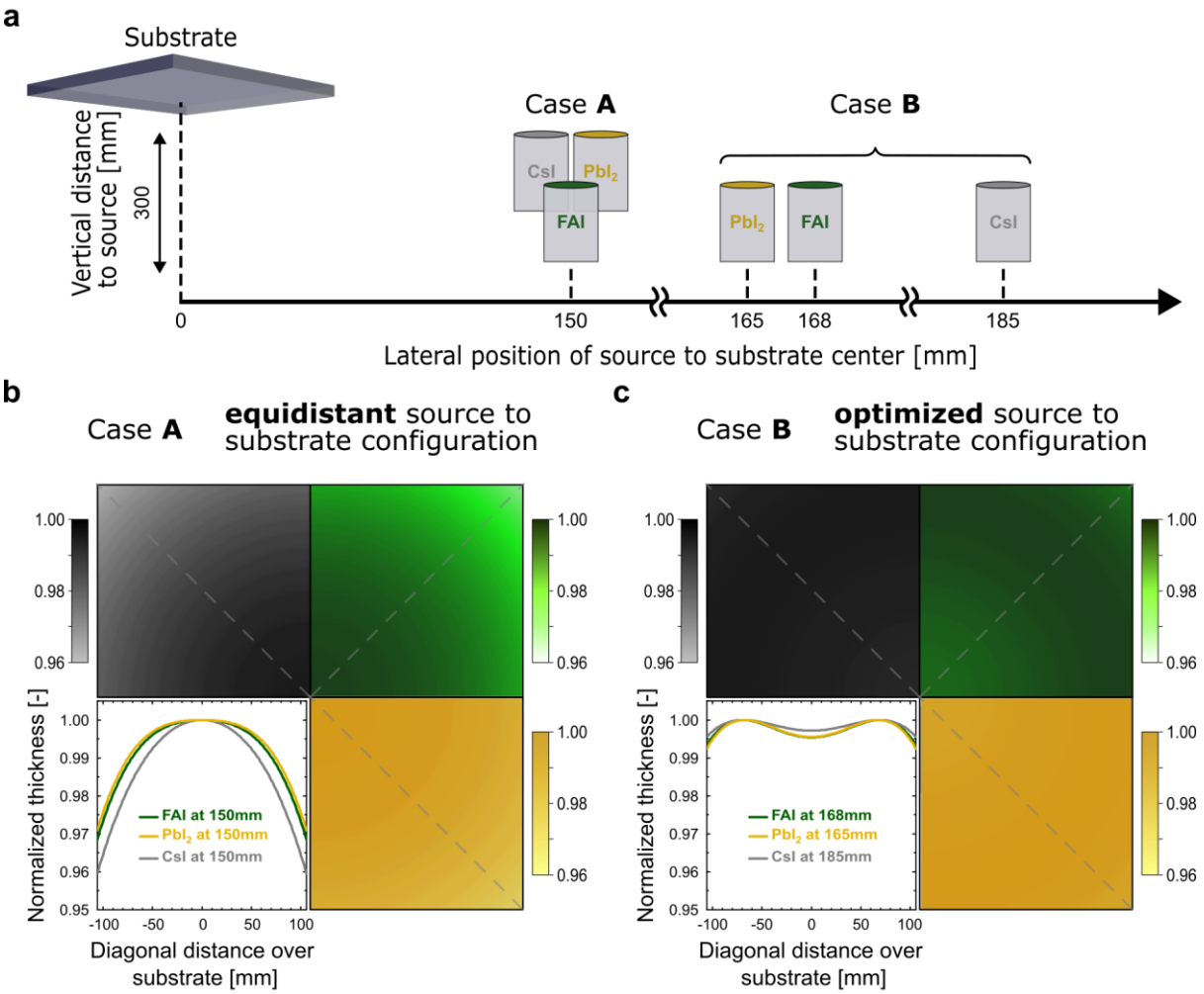


Figure 4: a Schematic of two different simulated source-to-substrate configurations with Case **A** = equidistant lateral source-to-substrate distances, and Case **B** = individually optimized lateral source-to-substrate distances. The vertical source-to-substrate distance is 300 mm. **b** Heatmaps of calculated thickness profile over a rotating substrate holder for CsI, FAI (mid particle size fraction) and PbI_2 at an equidistant lateral source-to-substrate distance of 150 mm. **c** Heatmaps of calculated thickness profile over a rotating substrate holder for CsI, FAI and PbI_2 with an individually optimized lateral source-to-substrate distance of 185 mm, 165 mm and 168 mm respectively.

In the case of multi-material deposition processes (co-deposition or sequential layer deposition), stoichiometric material ratios are crucial to form high-quality and homogeneous perovskite thin films. Therefore, variations in the optimal source-to-substrate distances for most homogeneous material deposition must be considered for optimized process control. However, conventional vacuum chambers do not allow for adjustment of the source position. To demonstrate the importance of our findings, we compare two simulated cases with different source-to-substrate distances for the exemplary selected precursor materials CsI, PbI_2 and FAI (only mid particle size fraction is considered here) using cylindrical crucibles. Case **A** uses an equidistant source-to-substrate arrangement with a lateral distance of 150 mm, which is comparable to the source-to-substrate distance used in our laboratory-scale thermal evaporation system, while Case **B**

considers the optimum case for most homogeneous deposition (see illustration in **Figure 4a**). The normalized diagonal profiles of each material show a diverging discrepancy between the three materials, with deviations of up to 4% from center to corner of the substrate as shown in **Figure 4b**. These discrepancies inevitably result in changes of material composition over the whole substrate. In comparison, Case **B** with the optimized source-to-substrate arrangement for most homogeneous deposition (compare **Figure 3f**) leads to minimized thickness deviations over the substrate for each individual precursor material of max. ~0.5% (see **Figure 4c**), resulting in a much more homogeneous material thickness ratio of all materials over the whole substrate. This demonstrates the importance of careful vacuum chamber design to increase compositional uniformity over the substrate. It should be noted that in a realistic co-deposition process, numerous additional parameters - such as chamber pressure, substrate temperature, and deposition rate - can also influence film growth and crystallization dynamics, thereby introducing further reproducibility challenges beyond those arising solely from the chamber design.[15,18–21]

A potential solution to our observations could be the implementation of sources with adjustable position to individually optimize the lateral source-to-substrate arrangements depending on each precursor material. This would result in increased homogeneity of deposited material thicknesses for different perovskite compositions. Our findings provide a clear indication that differences in the experimental setups and source arrangement inside the vacuum chambers of different laboratories complicate the transfer of process recipes and thus impede reproducibility between research groups.

3. Conclusion

In this work, the impact of FAI particle sizes and sublimation crucible geometry on the homogeneity of thermally sublimed perovskite films is analyzed for the first time. Changes in particle size distribution cause drastic changes in the directionality of the emitted vapor flux when depositing from conical crucibles. Furthermore, insufficient control of the used particle size fraction, strongly varying in commercial FAI precursor material, directly influences deposition homogeneity over the substrate, contributing to reported reproducibility problems for thermally sublimed PSCs. Comparison of conical and cylindrical crucible geometries and analysis of the resulting effect on the emitted vapor flux directionality shows a strong difference regarding beam-focusing properties. Deposition from cylindrical crucibles results in a much lower directionality of the emitted vapor flux, leading to an overall much more homogeneous deposition. Additionally, cylindrical crucibles are not affected by changes in the particle size

distribution of the used precursor material powder, making them a more promising candidate for reproducible vapor-based processing. Finally, an optimized source arrangement to minimize spatial deviations in material composition for a simulated multi-material deposition process is presented. Our findings highlight the importance of homogenizing precursor material, choice of crucible geometry and the design of thermal evaporation setups for reproducible fabrication of PSCs in vapor phase deposition processes, a critical factor for successful industrial realization of this promising technology.

4. Experimental Section/Methods

Materials

FAI (Greatcell Solar Materials, ≥99.99%), PbI_2 (TCI, 99.99%, trace metals basis), CsI (TCI, ≥99.0%)

Vacuum deposition setup

Physical vapor deposition of perovskite precursor materials was carried out in a nitrogen-filled glovebox integrated PEROvap vacuum system (M. Braun Inertgas-Systeme GmbH, Dresden). For each experiment, fresh precursor material (FAI: 1 g of respective fraction; PbI_2: 3 g; CsI: 3 g) was placed into cylindrical 10 cm³ crucibles (unless otherwise stated). The system was evacuated, reaching a base pressure of $<1.0 \cdot 10^{-5}$ mbar at the start of heating. A cooling inner surface surrounding all sublimation sources was maintained at -20 °C, and the substrate temperature was kept constant at 18 °C. Deposition was performed using a 300 mm vertical source–substrate distance, with the point source and substrate center positioned off-axis (~150 mm apart) without tilt or substrate rotation. The lateral distance from source to QCM was 75 mm, enabling scaling from thickness distribution to deposition rate profile. Deposition rates, monitored by individual QCMs, were maintained at FAI = 1.0 Å s^{-1}, PbI_2 = 13.5 Å s^{-1}, and CsI = 10.0 Å s^{-1} by automated rate control for FAI and manual adjustment of source temperature for PbI_2 and CsI. The corresponding temperature ranges for these deposition rates were ~140-160 °C for FAI, ~270-280 °C for PbI_2 and ~430-445 °C for CsI. We note that the measured temperatures depend a lot on the actual contact position of the thermocouple relative to the crucible and can therefore vary between systems.[22] Materials were used as received without further purification: FAI (GreatCell Solar, ≥99.99%), PbI_2 (TCI, 99.99% trace metals basis), and CsI (TCI, ≥99.0% titration).

Analysis and separation of different FAI particle size fractions

In order to analyze the particle size distribution of the FAI precursor material, analytical sieves with different mesh-sizes (800, 500, 200, 100, 50 µm) were used. We defined three main particle size fractions, namely "big" (x > 500 µm), "mid" (200 < x < 500 µm) and "small" (x < 200 µm).

Determination of layer thickness

The deposited layer thicknesses were determined using a White-Light-Interferometry (WLI) from Bruker (Bruker Contour GT-X500). Step height of the coated edges was detected using a combined mode of white light interferometry and phase shift imaging called UXI. A 5x magnification lens with an additional field of view lens of 0.55x were used to depict the edges. The working distance of the 5x objective is 6.7 mm. Light was set to values between 0.15 and 0.18%. Evaluation was done using the Vision64 Software of Bruker.

Fit-function

Function used to fit the thickness gradient of experimentally determined material thicknesses from a static deposition (for explicit derivation please see previously published work:[12]

$$t(x) = A \cdot \frac{cos^n\left(\arctan\left(\frac{x}{x_h}\right)\right)}{R^2} = A \cdot \frac{cos^n\left(\arctan\left(\frac{x}{x_h}\right)\right)}{x^2 + {x_h}^2}$$

with:

- **t(x)** = material thickness at a specific point x
- **x** = lateral distance of a specific point on substrate to emitting source
- $\mathbf{x_h}$ = height of the substrate holder in relation to the emitting source (in the used setup: $\mathbf{x_h}$ = 300 mm)
- **R** = distance from source to a point x on the substrate
- **A** = proportionality factor
- **n** = exponent of cosine law

Acknowledgements

A.D. and J.P. contributed equally to this work. This work was partly carried out with the support of the Karlsruhe Nano Micro Facility (KNMF, ID: 2025-033-032285) (www.kit.edu/knmf), a Helmholtz Research Infrastructure at Karlsruhe Institute of Technology (KIT). The authors gratefully acknowledge financial support by the Helmholtz Association (program-oriented funding phase IV, MTET Topic 1, Code: 38.01.02; Solar Technology Acceleration Platform (Solar TAP)), the Helmholtz European Partnering Program (TAPAS), the Helmholtz Energy Materials Foundry, the German Federal Ministry for Economic Affairs and Climate Action (BMWK) through the SHAPE project (03EE1123 A-E), the German Federal Ministry of Education and Research (BMBF) through the Zeitenwende Energy Security project and the Ministry of Science and Culture in the State of Lower Saxony through the program "zukunft.niedersachsen" (project NextGenPV). We acknowledge support by the Karlsruhe School of Optics & Photonics (KSOP) and the Ministry of Science, Research and Arts of Baden-Württemberg as part of the sustainability financing of the projects of the Excellence Initiative II. This work was partially funded by the European Union. Views and opinions expressed are however those of the author(s) only and do not necessarily reflect those of the European Union or RIA. Neither the European Union nor the granting authority can be held responsible for them. The NEXUS project has received funding from the European Union's Horizon Europe research and innovation program under grant agreement No. 101075330. Open access funding enabled and organized by Projekt DEAL.

Data Availability Statement

The data that support the findings of this study are available from the corresponding authors upon reasonable request.

Received: ((will be filled in by the editorial staff))
Revised: ((will be filled in by the editorial staff))
Published online: ((will be filled in by the editorial staff))

References

1 M. R. Filip, G. E. Eperon, H. J. Snaith and F. Giustino, *Nat Commun*, 2014, **5**, 5757.
2 E. L. Unger, L. Kegelmann, K. Suchan, D. Sörell, L. Korte and S. Albrecht, *J Mater Chem A Mater*, 2017, **5**, 11401–11409.

3 S. D. Stranks, G. E. Eperon, G. Grancini, C. Menelaou, M. J. P. Alcocer, T. Leijtens, L. M. Herz, A. Petrozza and H. J. Snaith, *Science (1979)*, 2013, **342**, 341–344.

4 S. De Wolf, J. Holovsky, S.-J. Moon, P. Löper, B. Niesen, M. Ledinsky, F.-J. Haug, J.-H. Yum and C. Ballif, *J Phys Chem Lett*, 2014, **5**, 1035–1039.

5 National Renewable Energy Laboratory (NREL), Best Research-Cell Efficiencies, https://www.nrel.gov/pv/cell-efficiency.html, (accessed 20 May 2025).

6 T. J. Jacobsson, A. Hultqvist, A. García-Fernández, A. Anand, A. Al-Ashouri, A. Hagfeldt, A. Crovetto, A. Abate, A. G. Ricciardulli, A. Vijayan, A. Kulkarni, A. Y. Anderson, B. P. Darwich, B. Yang, B. L. Coles, C. A. R. Perini, C. Rehermann, D. Ramirez, D. Fairen-Jimenez, D. Di Girolamo, D. Jia, E. Avila, E. J. Juarez-Perez, F. Baumann, F. Mathies, G. S. A. González, G. Boschloo, G. Nasti, G. Paramasivam, G. Martínez-Denegri, H. Näsström, H. Michaels, H. Köbler, H. Wu, I. Benesperi, M. I. Dar, I. Bayrak Pehlivan, I. E. Gould, J. N. Vagott, J. Dagar, J. Kettle, J. Yang, J. Li, J. A. Smith, J. Pascual, J. J. Jerónimo-Rendón, J. F. Montoya, J.-P. Correa-Baena, J. Qiu, J. Wang, K. Sveinbjörnsson, K. Hirselandt, K. Dey, K. Frohna, L. Mathies, L. A. Castriotta, Mahmoud. H. Aldamasy, M. Vasquez-Montoya, M. A. Ruiz-Preciado, M. A. Flatken, M. V. Khenkin, M. Grischek, M. Kedia, M. Saliba, M. Anaya, M. Veldhoen, N. Arora, O. Shargaieva, O. Maus, O. S. Game, O. Yudilevich, P. Fassl, Q. Zhou, R. Betancur, R. Munir, R. Patidar, S. D. Stranks, S. Alam, S. Kar, T. Unold, T. Abzieher, T. Edvinsson, T. W. David, U. W. Paetzold, W. Zia, W. Fu, W. Zuo, V. R. F. Schröder, W. Tress, X. Zhang, Y.-H. Chiang, Z. Iqbal, Z. Xie and E. Unger, *Nat Energy*, 2021, **7**, 107–115.

7 Y. Vaynzof, *Adv Energy Mater*, 2020, **10**, 2003073.

8 T. Abzieher, D. T. Moore, M. Roß, S. Albrecht, J. Silvia, H. Tan, Q. Jeangros, C. Ballif, M. T. Hoerantner, B.-S. Kim, H. J. Bolink, P. Pistor, J. C. Goldschmidt, Y.-H. Chiang, S. D. Stranks, J. Borchert, M. D. McGehee, M. Morales-Masis, J. B. Patel, A. Bruno and U. W. Paetzold, *Energy Environ Sci*, 2024, **17**, 1645–1663.

9 D. B. Ritzer, T. Abzieher, A. Basibüyük, T. Feeney, F. Laufer, S. Ternes, B. S. Richards, S. Bergfeld and U. W. Paetzold, *Progress in Photovoltaics: Research and Applications*, 2022, **30**, 360–373.

10 L. Gil-Escrig, M. Roß, J. Sutter, A. Al-Ashouri, C. Becker and S. Albrecht, *Solar RRL*, DOI:10.1002/solr.202000553.

11 F. U. Kosasih, E. Erdenebileg, N. Mathews, S. G. Mhaisalkar and A. Bruno, *Joule*, 2022, **6**, 2692–2734.

12 J. Petry, V. Škorjanc, A. Diercks, T. Feeney, A. Morsa, S. R. Kimmig, J. Baumann, F. Loeffler, S. Auschill, J. Damm, D. Baumann, F. Laufer, J. Kurpiers, M. Mueller, L. Korte, S. Albrecht, M. Roß, U. W. Paetzold and P. Fassl, *EES Solar*, DOI:10.1039/D5EL00069F.

13 S. Olthof and K. Meerholz, *Sci Rep*, 2017, **7**, 40267.

14 T. Abzieher, T. Feeney, F. Schackmar, Y. J. Donie, I. M. Hossain, J. A. Schwenzer, T. Hellmann, T. Mayer, M. Powalla and U. W. Paetzold, *Adv Funct Mater*, 2021, **31**, 2104482.

15 M. Roß, L. Gil-Escrig, A. Al-Ashouri, P. Tockhorn, M. Jošt, B. Rech and S. Albrecht, *ACS Appl Mater Interfaces*, 2020, **12**, 39261–39272.

16 T. Feeney, J. Petry, A. Torche, D. Hauschild, B. Hacene, C. Wansorra, A. Diercks, M. Ernst, L. Weinhardt, C. Heske, G. Gryn'ova, U. W. Paetzold and P. Fassl, *Matter*, 2024, **7**, 2066–2090.

17 A. Diercks, J. Petry, T. Feeney, R. Singh, T. Zhao, H. Hu, Y. Li, U. W. Paetzold and P. Fassl, *ACS Energy Lett*, 2025, 1165–1173.

18 K. L. Heinze, O. Dolynchuk, T. Burwig, J. Vaghani, R. Scheer and P. Pistor, *Sci Rep*, DOI:10.1038/s41598-021-94689-1.

19 A.-F. Castro-Méndez, F. Jahanbakhshi, D. K. LaFollette, B. J. Lawrie, R. Li, C. A. R. Perini, A. M. Rappe and J.-P. Correa-Baena, *J Am Chem Soc*, 2024, **146**, 18459–18469.

20 B. S. Kim, L. Gil-Escrig, M. Sessolo and H. J. Bolink, *Journal of Physical Chemistry Letters*, 2020, **11**, 6852–6859.

21 M. Kroll, S. D. Öz, Z. Zhang, R. Ji, T. Schramm, T. Antrack, Y. Vaynzof, S. Olthof and K. Leo, *Sustain Energy Fuels*, 2022, **6**, 3230–3239.

22 T. Feeney, A. Miaskiewicz, J. Petry, F. Laufer, R. Singh, S. Severin, V. Škorjanc, A. Diercks, S. Maniyarasu, L. Korte, S. Albrecht, U. W. Paetzold, M. Roß and P. Fassl, *Adv Funct Mater*, 2025, DOI:10.1002/adfm.202517873.

23 R. Heidrich, K. L. Heinze, S. Berwig, J. Ge, R. Scheer and P. Pistor, *Sci Rep*, DOI:10.1038/s41598-022-23132-w.

24 J. Emara, T. Schnier, N. Pourdavoud, T. Riedl, K. Meerholz and S. Olthof, *Advanced Materials*, 2016, **28**, 553–559.

25 J. Borchert, I. Levchuk, L. C. Snoek, M. U. Rothmann, R. Haver, H. J. Snaith, C. J. Brabec, L. M. Herz and M. B. Johnston, *ACS Appl Mater Interfaces*, 2019, **11**, 28851–28857.

26 K. P. S. Zanoni, L. Martínez-Goyeneche, C. Dreessen, M. Sessolo and H. J. Bolink, *Solar RRL*, DOI:10.1002/solr.202201073.

27 N. Rodkey, B. Huisman and H. J. Bolink, *Adv Eng Mater*, DOI:10.1002/adem.202400636.

28 B. Conings, J. Drijkoningen, N. Gauquelin, A. Babayigit, J. D'Haen, L. D'Olieslaeger, A. Ethirajan, J. Verbeeck, J. Manca, E. Mosconi, F. De Angelis and H. G. Boyen, *Adv Energy Mater*, DOI:10.1002/aenm.201500477.

29 M. Wang, S. Tan, Y. Zhao, P. Zhu, Y. Yin, Y. Feng, T. Huang, J. Xue, R. Wang, G. S. Han, H. S. Jung, J. Bian, J. W. Lee and Y. Yang, *Adv Funct Mater*, DOI:10.1002/adfm.202007520.

30 S. Hsiao, H. Lin, W. Lee, W. Tsai, K. Chiang, W. Liao, C. Ren-Wu, C. Chen and H. Lin, *Advanced Materials*, 2016, **28**, 7013–7019.

31 V. Held, N. Mrkyvkova, P. Nádaždy, K. Vegso, A. Vlk, M. Ledinský, M. Jergel, A. Chumakov, S. V. Roth, F. Schreiber and P. Siffalovic, *Journal of Physical Chemistry Letters*, 2022, **13**, 11905–11912.

32 M. M. Tavakoli, P. Yadav, D. Prochowicz, R. Tavakoli and M. Saliba, *J Phys D Appl Phys*, 2019, **52**, 034005.

33 R. Ji, Z. Zhang, C. Cho, Q. An, F. Paulus, M. Kroll, M. Löffler, F. Nehm, B. Rellinghaus, K. Leo and Y. Vaynzof, *J Mater Chem C Mater*, 2020, **8**, 7725–7733.

34 J. Feng, Y. Jiao, H. Wang, X. Zhu, Y. Sun, M. Du, Y. Cao, D. Yang and S. (Frank) Liu, *Energy Environ Sci*, 2021, **14**, 3035–3043.

35 M. Roß, S. Severin, M. B. Stutz, P. Wagner, H. Köbler, M. Favin-Lévêque, A. Al-Ashouri, P. Korb, P. Tockhorn, A. Abate, B. Stannowski, B. Rech and S. Albrecht, *Adv Energy Mater*, 2021, **11**, 2101460.

36 H. Li, J. Zhou, L. Tan, M. Li, C. Jiang, S. Wang, X. Zhao, Y. Liu, Y. Zhang, Y. Ye, W. Tress and C. Yi, *Sequential vacuum-evaporated perovskite solar cells with more than 24% efficiency*, 2022, vol. 8.

37 K. B. Lohmann, S. G. Motti, R. D. J. Oliver, A. J. Ramadan, H. C. Sansom, Q. Yuan, K. A. Elmestekawy, J. B. Patel, J. M. Ball, L. M. Herz, H. J. Snaith and M. B. Johnston, *ACS Energy Lett*, 2022, **7**, 1903–1911.

38 I. Susic, A. Kama, L. Gil-Escrig, C. Dreessen, F. Palazon, D. Cahen, M. Sessolo and H. J. Bolink, *Adv Mater Interfaces*, DOI:10.1002/admi.202202271.

39 Q. Yuan, K. B. Lohmann, R. D. J. Oliver, A. J. Ramadan, S. Yan, J. M. Ball, M. G. Christoforo, N. K. Noel, H. J. Snaith, L. M. Herz and M. B. Johnston, *ACS Appl Mater Interfaces*, 2023, **15**, 772–781.

40 Y. H. Chiang, K. Frohna, H. Salway, A. Abfalterer, L. Pan, B. Roose, M. Anaya and S. D. Stranks, *ACS Energy Lett*, 2023, **8**, 2728–2737.

41 D. Lin, J. Fang, X. Yang, X. Wang, S. Li, D. Wang, G. Xie, H. Li, X. Wang and L. Qiu, *Small*, 2024, **20**, 2307960.

42 Y. Y. Xu, Y. Jiang, H. Q. Du, X. Gao, Z. Y. Qiang, C. X. Wang, Z. W. Tao, L. H. Yang, R. Zhi, G. J. Liang, H. Y. Cai, M. U. Rothmann, Y. B. Cheng and W. Li, *Adv Funct Mater*, DOI:10.1002/adfm.202312037.

43 S. Yan, J. B. Patel, J. E. Lee, K. A. Elmestekawy, S. R. Ratnasingham, Q. Yuan, L. M. Herz, N. K. Noel and M. B. Johnston, *ACS Energy Lett*, 2023, **8**, 4008–4015.

44 S. Zou, S. Liang, T. Yu, J. Su, Y. Jiang, R. Hua, Z. Huang, W. Zhang, L. Shi, Y. Guo, Q. Dong, Y. Han, H. Ma, Y. Gao, Y. Shi and Y. Dong, *Mater Today Energy*, 2024, **40**, 101506.

45 M. R. Leyden, V. Škorjanc, A. Miaskiewicz, S. Severin, S. Maniyarasu, T. Gries, J. Beckedahl, F. Scheler, M. Simmonds, P. Holzhey, J. Kurpiers, L. Korte, M. Roß and S. Albrecht, *Solar RRL*, 2024, **8**, 2400575.

46 C. J. Shih, Y. S. Chen, D. Luo, C. W. Yu, K. H. Chen, G. Murokinas, Y. C. Huang, C. F. Li, Y. C. Huang and S. W. Liu, *Solar Energy*, DOI:10.1016/j.solener.2024.112872.

47 J. Zhou, L. Tan, Y. Liu, H. Li, X. Liu, M. Li, S. Wang, Y. Zhang, C. Jiang, R. Hua, W. Tress, S. Meloni and C. Yi, *Joule*, 2024, **8**, 1691–1706.

48 A. G. Kuba, F. Sahli, M. Othman, K. Artuk, Q. Jeangros, A. Hessler-Wyser, C. Ballif and C. M. Wolff, *ACS Energy Lett*, 2025, 2710–2717.

49 R. A. Nambiar, D. P. McMeekin, M. K. Czenry, J. A. Smith, M. Taddei, P. Caprioglio, A. Kumar, B. W. Putland, J. Wang, K. A. Elmestekawy, A. Dasgupta, S. Seo, M. G. Christoforo, J. Yao, D. J. Graham, L. M. Herz, D. Ginger and H. J. Snaith, *EES Solar*, 2025, **1**, 129–138.

50 I. Susic, L. Gil-Escrig, F. Palazon, M. Sessolo and H. J. Bolink, *ACS Energy Lett*, 2022, **7**, 1355–1363.

51 L. Gil-Escrig, C. Dreessen, F. Palazon, Z. Hawash, E. Moons, S. Albrecht, M. Sessolo and H. J. Bolink, *ACS Energy Lett*, 2021, **6**, 827–836.

52 L. Gil-Escrig, C. Dreessen, I. C. Kaya, B.-S. Kim, F. Palazon, M. Sessolo and H. J. Bolink, *ACS Energy Lett*, 2020, **5**, 3053–3061.

53 H. Li, L. Tan, C. Jiang, M. Li, J. Zhou, Y. Ye, Y. Liu and C. Yi, *Adv Funct Mater*, 2023, **33**, 2211232.

54 J. Petry, V. Škorjanc, A. Diercks, T. Feeney, A. Morsa, S. R. Kimmig, J. Baumann, F. Löffler, S. Auschill, J. Damm, D. Baumann, F. Laufer, J. Kurpiers, M. Müller, L. Korte, S. Albrecht, M. Roß, U. W. Paetzold and P. Fassl, *EES Solar*, 2025, **1**, 404–418.

Supporting Information

Supporting Information is available from the Wiley Online Library or from the author.

The table of contents entry should be 50–60 words long and should be written in the present tense. The text should be different from the abstract text.

Particle Size Matters – Impact of Particle Size and Crucible Geometry on Sublimation Behavior of Formamidinium Iodide

FAI precursor particle size and sublimation crucible geometry critically determine vapor flux directionality and deposition uniformity in thermal sublimation processes. Conical crucibles exhibit particle-size-dependent beam focusing, while cylindrical crucibles show a much more homogeneous deposition due to de-focusing effects of the emitted vapor flux. These findings demonstrate the importance of careful vacuum chamber design for repeatable vapor phase deposition.

